

Density diagnostics of ionized outflows in active galactic nuclei X-ray and UV absorption lines from metastable levels in Be-like to C-like ions

Junjie Mao^{1, 2}, J. S. Kaastra^{1, 2}, M. Mehdipour¹, A. J. J. Raassen^{1, 3}, Liyi Gu¹, J. M. Miller⁴

¹ SRON Netherlands Institute for Space Research, Sorbonnelaan 2, 3584 CA Utrecht, the Netherlands
e-mail: J.Mao@sron.nl

² Leiden Observatory, Leiden University, Niels Bohrweg 2, 2300 RA Leiden, the Netherlands

³ Astronomical Institute “Anton Pannekoek”, University of Amsterdam, Science Park 904, 1098 XH Amsterdam, the Netherlands

⁴ Department of Astronomy, University of Michigan, 1085 South University Avenue, Ann Arbor, MI 48109-1107, USA

Received date / Accepted date

ABSTRACT

Context. Ionized outflows in Active Galactic Nuclei (AGN) are thought to influence their nuclear and local galactic environment. However, the distance of the outflows with respect to the central engine is poorly constrained, which limits our understanding of their kinetic power as a cosmic feedback channel. Therefore, the impact of AGN outflows on their host galaxies is uncertain. However, when the density of the outflows is known, their distance can be immediately obtained from their modelled ionization parameter.

Aims. A theoretical study of density diagnostics of ionized outflows using absorption lines from metastable levels in Be-like to C-like cosmic abundant ions.

Methods. With the new self-consistent PhotoIONization (PION) model in the SPEX code, we are able to calculate detailed level populations, including the ground and metastable levels. This enables us to determine under what physical conditions the metastable levels are significantly populated. We then identify characteristic lines from these metastable levels in the 1 – 2000 Å wavelength range.

Results. In the large density range of $n_H \in (10^6, 10^{20}) \text{ m}^{-3}$, the metastable levels $2s2p$ ($^3P_{0-2}$) in Be-like ions can be significantly populated. For B-like ions, merely the first excited level $2s^22p$ ($^2P_{3/2}$) can be used as a density probe. For C-like ions, the first two excited levels $2s^22p^2$ (3P_1 and 3P_2) are better density probes than the next two excited levels $2s^22p^2$ (1S_0 and 1D_2). Different ions in the same isoelectronic sequence cover not only a wide range of ionization parameter, but also a wide range of density. On the other hand, within the same isonuclear sequence, less ionized ions probe lower density and smaller ionization parameter. Finally, we re-analyzed the high-resolution grating spectra of NGC 5548 observed with *Chandra* in January 2002, using a set of PION components to account for the ionized outflow. We derive lower (or upper) limits of plasma density in five out of six PION components, based on the presence (or absence) of the metastable absorption lines. Once atomic data from N-like to F-like ions are available, combined with the next generation of spectrometers, which cover both X-ray and UV wavelength range with higher spectral resolution and larger effective area, tight constraints on the density, and thus the location and kinetic power of AGN outflows can be obtained.

Key words. plasma – atomic data – atomic processes – techniques: spectroscopic – X-rays: galaxies – galaxies: active – galaxies: Seyfert – galaxies: individual: NGC 5548

1. Introduction

AGN outflows may play an important role in the cosmic feedback (see e.g. Fabian 2012, for a review). For an outflow in a thin spherical shell geometry moving constantly with a radial velocity v , the mass outflow rate can be estimated via

$$\dot{M}_{\text{out}} = 1.43 m_p N_H v \Omega \left(\frac{r^2}{\Delta r} \right), \quad (1)$$

where m_p is the proton mass, N_H the hydrogen column density along the line of sight, r the distance between the outflow and the central engine, Δr the radial size of the outflow, and Ω the solid angle subtended by the outflow. The kinetic power carried by the outflow is $L_{\text{KE}} = \frac{1}{2} \dot{M}_{\text{out}} v^2$. Thus, distant and/or high-velocity outflow leads to larger mass outflow rate (\dot{M}_{out}) and kinetic power (L_{KE}).

While the line of sight hydrogen column density (N_H) and velocity (v) of the outflow can be well constrained via spectral analysis, its solid angle (Ω) and location (r) are the main source of uncertainties in estimating the kinetic power that impacts the

host galaxy. The solid angle highly depends on the exact geometry, which is not investigated here. On the other hand, the location can be immediately obtained via the definition of the ionization parameter¹ (Tarter et al. 1969; Krolik et al. 1981), if the density of the outflow is known,

$$\xi = \frac{L}{n_H r^2} \quad (2)$$

where L is the 1–1000 Ryd (or 13.6 eV–13.6 keV) band luminosity of the ionizing source, n_H the hydrogen number density of the ionized plasma and r the distance of the plasma with respect to the ionizing source.

However, it is not trivial to determine the density of a photoionized plasma. Three different approaches have been used for measuring the density of AGN outflows. The first approach is a timing analysis where one monitors the response of the ionized outflow to changes in the ionizing continuum. A high-density

¹ Throughout this paper, ξ is in units of 10^{-9} W m (i.e. $\text{erg s}^{-1} \text{ cm}$).

plasma recombines more rapidly, thus yields a shorter recombination timescale. This approach has been used to constrain density in Mrk 509 (Kaastra et al. 2012), NGC 5548 (Ebrero et al. 2016), and NGC 4051 (Silva et al. 2016), etc. The timing analysis is in general challenging, since the observations of a given object are often sparse, washing out possible effects of variability, and lacking the signal-to-noise ratio required to significantly measure the expected changes (Ebrero et al. 2016).

The second approach is a spectral analysis of density sensitive emission lines. It is well known that the inter-combination to forbidden emission line ratio in the He-like triplets (e.g. Porquet et al. 2010) varies for plasmas with different density. This density probe, observed in the X-ray wavelength range, has been applied to a few AGNs, e.g. NGC 4051 (Collinge et al. 2001), NGC 4593 (McKernan et al. 2003) and NGC 4151 (Schurch et al. 2004), where upper limits of the plasma density are derived. Meanwhile, as shown in Mehdipour et al. (2015a), line absorption of He-like ion triplet lines by Li-like ions make density diagnostics complicated. In addition, for solar corona studies, metastable emission lines observed in the EUV wavelength range from Be-like (Landi & Miralles 2014), B-like (Keenan et al. 1998; Ciaravella et al. 2001; Gallagher et al. 1999; Warren & Brooks 2009), C-like (Keenan et al. 1993; Landi & Landini 1998) and N-like (Keenan et al. 2004) ions are widely used to determine the density.

The third approach is a spectral analysis where one measures absorption lines from density sensitive metastable levels. This method has been successfully used for absorption lines observed in the UV band (e.g. Arav et al. 2015). In the X-ray band, Kaastra et al. (2004) obtain an upper limit of the outflow density in Mrk 279, with the density sensitive metastable absorption transitions $2s^2-1s2s^22p$ in O V (Be-like) ~ 22.4 Å. Later, King et al. (2012) reported an upper limit of the outflow density in NGC 4051, using the ground (11.77 Å) and metastable (11.92 Å) transitions in Fe XXII (B-like). The same transitions in Fe XXII was in fact previously used by Miller et al. (2008) in the stellar mass black hole GRO J1655–40, yielding a tight constraint on the density of a disk wind.

In this work, we carry out a systematic study of density diagnostics with ions in different isoelectronic sequences in photoionized equilibrium. Detailed calculation is done with our new photoionized plasma model PION² in the SPEX code (Kaastra et al. 1996). Given cosmic abundances (the proto-solar abundance table in Lodders et al. 2009), we consider elements including C, N, O, Ne, Mg, Si, S, Ar, Ca, and Fe. Throughout this paper, we consider plasma densities in the range between 10^6 m⁻³ (or 1 cm⁻³) and 10^{20} m⁻³ (or 10^{14} cm⁻³). At $n_H = 10^{20}$ m⁻³, metastable levels in Be-like to F-like ions can be significantly populated compared to the population of the ground level, while for Li-like, Ne-like and Na-like ions, no metastable levels are significantly populated. Therefore, we focus on Be-like to C-like ions in Section 3.1 to 3.3. Due to the lack of atomic data, for N-like to F-like ions, we merely discuss Fe XX, Fe XIX and Fe XVIII in Appendix A.

2. Methods

Unless specified otherwise, we use the spectral energy distribution (SED) of NGC 5548 in our photoionization modelling, i.e. the AGN1 SED shown in Fig. 1 of Mehdipour et al. (2016). The

² An introduction of PION and comparison to other photoionization codes can be found in Mehdipour et al. (2016)

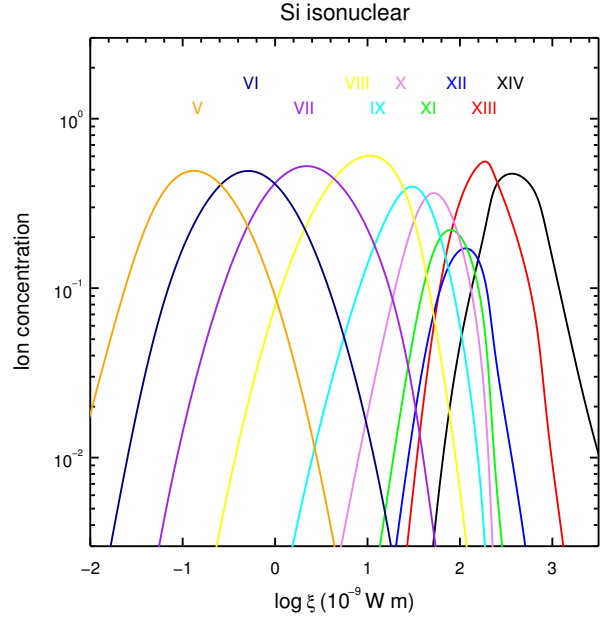


Fig. 1. Ion concentration of Si isonuclear sequence (H-like to Ne-like) as a function of the ionization parameter (in units of 10^{-9} W m, i.e. $\text{erg s}^{-1} \text{cm}$).

photoionized outflow is assumed to be optically thin with a slab geometry. The line of sight hydrogen column density (N_H) is 10^{24} m⁻². The covering factor is unity. No velocity shift with respect to the central engine is assumed here, and the turbulent velocity is set to 100 km s⁻¹ in the calculation.

When modelling a photoionized plasma with our new PION model in the SPEX code, its thermal equilibrium, ionization balance and level population are calculated self-consistently with detailed atomic data of relevant collisional and radiative processes, such as collisional excitation and de-excitation (FAC calculation, Gu 2008), radiative recombination (Badnell 2006; Mao & Kaastra 2016), inner shell ionization (Urdampilleta et al. 2017), etc. The thermal balance and instability curve are shown in Fig. 3–5 of Mehdipour et al. (2016). Ion concentrations are derived accordingly, and we show in Figure 1 the ion concentrations of Si XIV (H-like) to Si V (Ne-like) as a function of the ionization parameter. The level population is also calculated simultaneously.

3. Results

In Section 3.1 (for Be-like ions) to Section 3.3 (for C-like ions), we first show which metastable levels (Table 1) can be significantly populated in a large density range of $n_H \in (10^6, 10^{20})$ m⁻³. Note that different ionization parameters are used to maximize the ion concentration of different ions, e.g. $\log_{10}(\xi) = 1.90$ for Si XI (Be-like), $\log_{10}(\xi) = 2.0$ for Si XII (B-like), and $\log_{10}(\xi) = 2.1$ for Ar XIII (C-like), respectively. Secondly, we list characteristic absorption lines from these metastable levels. Absorption lines from the ground level are listed together with density sensitive lines from the metastable levels, so that one can tell whether the spectral resolution of a certain instrument is fine enough to distinguish these lines. If so, these lines can be used for density diagnostics.

Table 1. Level indices for the ground level (Level 1) and density sensitive metastable levels (Level 2-5) from the Be-like to F-like isoelectronic sequences.

Index	1		2		3		4		5	
Sequence	Conf.	$^{2S+1}L_J$	Conf.	$^{2S+1}L_J$	Conf.	$^{2S+1}L_J$	Conf.	$^{2S+1}L_J$	Conf.	$^{2S+1}L_J$
Be-like	$2s^2$	1S_0	$2s2p$	3P_0	$2s2p$	3P_1	$2s2p$	3P_2	--	--
B-like	$2s^22p$	$^2P_{1/2}$	$2s^22p$	$^2P_{3/2}$	--	--	--	--	--	--
C-like	$2s^22p^2$	3P_0	$2s^22p^2$	3P_1	$2s^22p^2$	3P_2	$2s^22p^2$	1D_2	$2s^22p^2$	1S_0
N-like (Fe)	$2s^22p^3$	$^4S_{3/2}$	$2s^22p^3$	$^2D_{3/2}$	$2s^22p^3$	$^2D_{5/2}$	$2s^22p^3$	$^2P_{1/2}$	$2s^22p^3$	$^2P_{3/2}$
O-like (Fe)	$2s^22p^4$	3P_2	$2s^22p^4$	3P_0	$2s^22p^4$	3P_1	$2s^22p^4$	1D_2	$2s^22p^4$	1S_0
F-like (Fe)	$2s^22p^5$	$^2P_{3/2}$	$2s^22p^5$	$^2P_{1/2}$	--	--	--	--	--	--

Notes. “Conf.” is short for electron configuration. $^{2S+1}L_J$ refers to the spectroscopic notations, where S is the total spin quantum number ($2S + 1$ is the spin multiplicity), L is the total orbital quantum number and J is the total angular momentum quantum number.

3.1. Be-like

Figure 2 shows the metastable to ground level population ratios as a function of plasma density. The lifetime of the first excited level $1s^22s2p$ (3P_0) is rather long, so that even if the plasma density is rather low, the metastable level can still be populated up to a few percent of the ground level population. Accordingly, a plateau can be found in the $^3P_0/{}^3S_0$ level population ratio (left panel of Figure 2). The third excited level $1s^22s2p$ (3P_2) can be more easily populated at lower density, compared to the second excited level $1s^22s2p$ (3P_1). The rest of the excited levels in Be-like ions are not significantly populated ($< 0.01\%$ of the ground level population) in a photoionized plasma with density $n_H \lesssim 10^{20} \text{ m}^{-3}$.

Given that the metastable levels (Level 2-4) can be populated up to 20% of the ground level (Level 1) population, we list in Table 2 three sets of characteristic transitions ($n_j = 2 - 2$, $2 - 3$, and $1 - 2$) for each level. Corresponding wavelength (λ) and oscillator strength (f) of these absorption features in the X-ray ($1 - 100 \text{ \AA}$) and UV ($100 - 2000 \text{ \AA}$) wavelength range are listed as well.

Among the three transitions of each level in the same ion, the inner shell $1s - 2p$ transition (denoted as $n_j = 1 - 2$) always yields the shortest wavelength, while the $2s - 2p$ transition ($n_j = 2 - 2$) yields the longest wavelength. There are of course more transitions than we listed in Table 2. For instance, there are in total six $1s^22s2p$ (3P) – $1s^22p^2$ (3P) metastable transitions around $\lambda \sim 1175 \text{ \AA}$ for C III, which have been successfully used for density diagnostic in AGN ionized outflows (e.g. Arav et al. 2015). Transitions with larger oscillator strengths (f) are listed in Table 2 for simplicity. For the six C III $\lambda \sim 1175 \text{ \AA}$ lines, the three tabulated lines have $f > 0.1$, while the other three lines have slightly smaller oscillator strengths.

For all three sets of transitions, the metastable to ground separation ($\Delta\lambda = |\lambda_{2,3,4} - \lambda_1|$) increases with increasing wavelength of the lines. For the inner shell transitions, the separations are rather small with $\Delta\lambda(n_j = 1 - 2) \lesssim 0.14 \text{ \AA}$. For the other two sets of transitions, the separations are relatively large, ranging from $\sim 0.3 \text{ \AA}$ (for $\lambda \sim 10 \text{ \AA}$) to $\sim 200 \text{ \AA}$ (for $\lambda \sim 1000 \text{ \AA}$), which are larger than the spectral resolution of current X-ray grating spectrometers. The metastable lines themselves, on the other hand, are closer to each other ($\lesssim 0.2 \text{ \AA}$ for lines in the X-ray band and $\lesssim 3 \text{ \AA}$ for lines in the UV band). This is simply due to the fact that the three metastable levels are the fine structure splitting of the same 3P term.

3.2. B-like

For B-like ions, only the first excited level $2s^22p$ ($^2P_{3/2}$) can be significantly populated up to a factor of two above the ground level population, as shown in Figure 3. None of the rest of the excited levels are significantly populated ($< 0.01\%$ of the ground level population) in a photoionized plasma with density $n_H \lesssim 10^{20} \text{ m}^{-3}$. At sufficient high density, the metastable to ground level population ratio follows the Boltzmann distribution (meanwhile the plasma is partially in local temperature equilibrium).

Characteristic absorption lines from the ground (Level 1) and metastable level (Level 2) in B-like ions are listed in Table 3. Similar to the Be-like isoelectronic sequence (Section 3.1), among the three transitions for the same ion, the inner shell transition ($n_j = 1 - 2$) has the shortest wavelength, the $n_j = 2 - 2$ transition has the longest wavelength. The metastable to ground separation ($\Delta\lambda$) is negligible for the inner shell transition ($n_j = 1 - 2$). For the other two sets of transitions, the separations between the ground and metastable lines are $\Delta\lambda(n_j = 2 - 3) \sim 0.15 - 0.30 \text{ \AA}$ and $\Delta\lambda(n_j = 2 - 2) \sim 0.2 - 2.7 \text{ \AA}$, respectively, which are larger than the spectral resolution of current X-ray grating spectrometers (e.g. Table 1 in Kaastra et al. 2017).

3.3. C-like

For C-like ions, the first two excited levels $2s^22p^2$ (3P_1 and 3P_2) can be significantly populated up to a factor of a few of the ground level population, as shown in Figure 4. The next two excited levels $2s^22p^2$ (1D_2 and 1S_0) can also be populated up to tens of percent of the ground level population. The rest of the excited levels are not significantly populated ($< 0.01\%$ of the ground level population) in a photoionized plasma with density $n_H \lesssim 10^{20} \text{ m}^{-3}$.

Since the metastable level $2s^22p^2$ (1S_0) is only significantly populated at rather high density (the right most panel in Figure 4), for simplicity, only transitions from the ground (Level 1) and the first three metastable levels (Level 2 – 4) are listed in Table 4. Again, the inner shell transition ($n_j = 1 - 2$) corresponds to the line with the shortest wavelength, and the $n_j = 2 - 2$ transition corresponds to the line with the longest wavelength. For the inner shell transition, the ground to metastable separation ($\Delta\lambda$) is negligible. For the other two transitions ($n_j = 2 - 2$ and $2 - 3$) that we listed here, it is easier (with $\Delta\lambda \gtrsim 0.1 \text{ \AA}$) to distinguish lines from the ground $2s^22p^2$ (3P_0) and lines from the third ex-

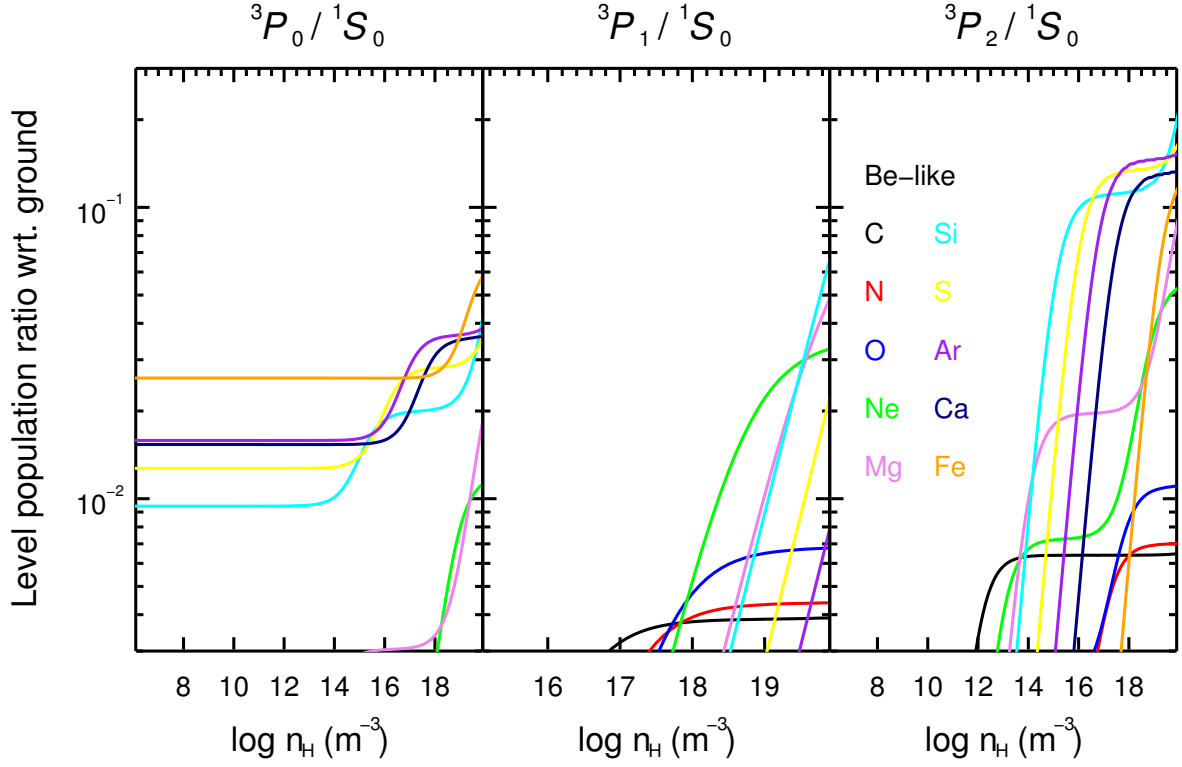


Fig. 2. Level population ratios as a function of plasma density (in the range of 10^{6-20}m^{-3} or 10^{0-14}cm^{-3}), at ionization parameter of maximum ion concentration in the ionization balance. The configuration of the ground (1S_0) and metastable levels ($^3P_{0-2}$) are listed in Table 1.

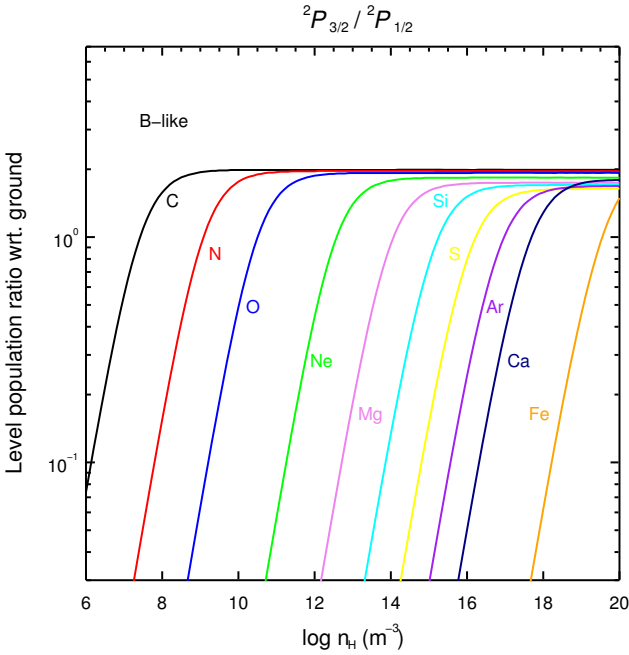


Fig. 3. Similar to Figure 2 but for B-like ions.

cited level $2s^2 2p^2 (^1D_2)$. Lines from the ground and the first two excited levels are close to each other since the lower levels are the fine structure splitting of the same term 3P . Between the $n_j = 2-3$ and $n_j = 2-2$ transitions, it is more difficult to distinguish lines from the ground and the first two excited levels for

the former, e.g. CI lines around $\lambda \sim 1277 \text{ \AA}$, NII lines around $\lambda \sim 533 \text{ \AA}$.

3.4. Summary

For Be-like ions, the first three excited levels $2s2p (^3P_{0-2})$ can be significantly populated ($\geq 1\%$ of the ground level population) when $n_H \gtrsim 10^{14} \text{ m}^{-3}$. Moreover, the third excited level $2s2p (^3P_2)$ can be populated more easily at such a high density. For B-like ions, merely the first excited level $2s^2 2p (^2P_{3/2})$ can be used as a density probe. For C-like ions, the metastable levels $2s^2 2p^2 (^3P_1$ and $^3P_2)$ can be more easily populated than $2s^2 2p^2 (^1D_2$ and $^1S_0)$. On the other hand, the transition from the $2s^2 2p^2 (^1D_2)$ level can be more easily distinguished from the transition from the ground level $2s^2 2p^2 (^3P_0)$.

The metastable levels in Be-like ions are less populated compared to B-like and C-like ions at the same density. For all three isoelectronic sequences, it is rather difficult to distinguish inner shell transitions from the ground and metastable levels.

The wavelengths and oscillator strengths can be obtained from SPEX atomic code and table (SPEXACT) v3.04. We cross-checked the wavelengths of the lines in Table 2 to 4 with those from NIST v5.3 (Kramida et al. 2015) if available.

4. Discussion

4.1. Ionization parameter dependence

In Section 3, for each ion, the level population is calculated given a certain ionization parameter. Here we discuss the level population dependence on both ionization parameter and density. Since the majority of the $n_j = 2-2$ and $n_j = 2-3$ transitions from ions

Table 2. Characteristic absorption lines from the ground and the metastable levels in Be-like ions.

Index	1		2		3		4	
n_j	Lower	Upper	Lower	Upper	Lower	Upper	Lower	Upper
2 – 2	$2s^2 (^1S_0)$	$2s2p (^1P_1)$	$2s2p (^3P_0)$	$2p^2 (^3P_1)$	$2s2p (^3P_1)$	$2p^2 (^3P_2)$	$2s2p (^3P_2)$	$2p^2 (^3P_2)$
Ion	λ (Å)	f	λ (Å)	f	λ (Å)	f	λ (Å)	f
C III	977.012	0.76	1175.254	0.27	1174.923	0.11	1175.702	0.20
N IV	765.141	0.61	922.511	0.22	921.986	0.09	923.212	0.17
O V	629.727	0.50	759.436	0.19	758.671	0.08	760.440	0.14
Ne VII	465.216	0.41	559.944	0.16	558.605	0.07	561.724	0.12
Mg IX	368.068	0.31	441.196	0.12	439.173	0.05	443.969	0.09
Si XI	303.323	0.27	361.410	0.10	358.650	0.04	365.431	0.08
S XIII	256.683	0.24	303.382	0.09	299.954	0.04	308.950	0.07
Ar XV	221.133	0.21	258.764	0.08	254.827	0.04	266.239	0.06
Ca XVII	192.818	0.19	223.018	0.08	218.821	0.03	232.827	0.05
Fe XXIII	132.906	0.15	147.270	0.06	144.389	0.03	166.689	0.03
n_j	Lower	Upper	Lower	Upper	Lower	Upper	Lower	Upper
2 – 3	$2s^2 (^1S_0)$	$2s3p (^1P_1)$	$2s2p (^3P_0)$	$2s3d (^3D_1)$	$2s2p (^3P_1)$	$2s3d (^3D_2)$	$2s2p (^3P_2)$	$2s3d (^3D_3)$
Ion	λ (Å)	f	λ (Å)	f	λ (Å)	f	λ (Å)	f
C III	386.200	0.23	459.463	0.56	459.510	0.42	459.624	0.47
N IV	247.203	0.33	283.415	0.61	283.463	0.46	283.572	0.51
O V	172.168	0.38	192.749	0.63	192.795	0.47	192.902	0.53
Ne VII	97.495	0.47	106.040	0.68	106.085	0.51	106.189	0.57
Mg IX	62.751	0.53	67.089	0.72	67.134	0.54	67.239	0.61
Si XI	43.763	0.46	46.362	0.73	46.298	0.54	46.399	0.61
S XIII	32.242	0.38	33.806	0.74	33.852	0.55	33.951	0.61
Ar XV	24.759	0.32	25.808	0.75	25.850	0.56	25.953	0.62
Ca XVII	19.558	0.36	20.310	0.78	20.339	0.56	20.437	0.62
Fe XXIII	10.980	0.41	11.298	0.74	11.325	0.54	11.441	0.61
n_j	Lower	Upper	Lower	Upper (†)	Lower	Upper (†)	Lower	Upper (†)
1 – 2	$2s^2 (^1S_0)$	$1s2s2p (^1P_1)$	$2s2p (^3P_0)$	$1s2s2p^2 (^3P_1)$	$2s2p (^3P_1)$	$1s2s2p^2 (^3P_2)$	$2s2p (^3P_2)$	$1s2s2p^2 (^3P_2)$
Ion	λ (Å)	f	λ (Å)	f	λ (Å)	f	λ (Å)	f
C III	42.165	0.62	42.385	0.31	42.384	0.13	42.385	0.23
N IV	29.941	0.65	30.088	0.33	30.086	0.14	30.088	0.24
O V	22.360	0.61	22.474	0.30	22.472	0.13	22.474	0.22
Ne VII	13.820	0.66	13.878	0.35	13.877	0.16	13.879	0.22
Mg IX	9.378	0.68	9.410	0.44	9.413	0.26 (3D_2)	9.415	0.15 (3D_3)
Si XI	6.776	0.70	6.798	0.52 (3D_1)	6.799	0.27 (3D_2)	6.797	0.27
S XIII	5.123	0.71	5.137	0.56 (3D_1)	5.138	0.27 (3D_2)	5.136	0.28
Ar XV	4.007	0.72	4.017	0.57 (3D_1)	4.018	0.27 (3D_2)	4.016	0.29
Ca XVII	3.222	0.72	3.228	0.59 (3D_1)	3.228	0.28 (3D_2)	3.228	0.29
Fe XXIII	1.870	0.69	1.873	0.61	1.874	0.29 (3D_2)	1.874	0.26

Notes. For the $1s - 2p$ transitions (denoted as $n_j = 1 - 2$) from the metastable (lower) levels, the upper levels (denoted as †) vary ($^3P_{1-2}$ or $^3D_{1-3}$) for different elements (exceptions are marked following the f -values).

in the same isoelectronic sequence share the same lower and upper levels (Table 2 to 4), we take these transitions from Be-like Si XI to C-like Si IX for this exercise. The ionization dependence can be applied to the rest of the ions in the same sequence. Note that inner shell transitions ($n_j = 1 - 2$) are excluded since it is difficult to distinguish lines from ground and metastable levels anyway (Section 3.4). We choose three different ionization parameters for each ion, corresponding to the maximum ion concentration and $\sim 90\%$ of the maximum ion concentration.

As shown in Figure 5, the optical depth at the line centre ($\tau_0 \propto N_i f$) varies with ionization parameter and density. Similarly, the metastable to ground equivalent width ratios ($EW_{\text{meta}}/EW_{\text{ground}}$) involving the $2s2p (^3P_2)$ metastable level in

Be-like ions and the $2s^22p^2 (^1D_2)$ metastable level in C-like ions are sensitive to both ionization parameter and density of the plasma. Nonetheless, the metastable to ground equivalent width ratios involving the $2s^22p (^2P_{3/2})$ metastable level in the B-like sequence and the $2s^22p^2 (^3P_1)$ and 3P_2 metastable levels in the C-like sequence are only sensitive to the density of the plasma, which makes them ideal density probes.

We caution that adopting a different ionizing SED yields a different ionization balance for the plasma. That is to say, the exact value of the ionization parameters where the ion concentration reaches maximum or 90% of the maximum in Figure 6 differs for different SEDs (Table 5). The SED adopted here is representative for a typical Seyfert 1 galaxy. Of course, the ex-

Table 3. Characteristic absorption lines from the ground and metastable level in B-like ions.

Index	1		2	
n_j	Lower	Upper (†)	Lower	Upper
2 – 2	$2s^22p (^2P_{1/2})$	$2s2p^2 (^2P_{1/2})$	$2s^22p (^2P_{3/2})$	$2s2p^2 (^2P_{3/2})$
Ion	λ (Å)	f	λ (Å)	f
C II	903.962	0.33	904.142	0.42
N III	685.515	0.28	685.818	0.36
O IV	554.076	0.23	554.514	0.29
Ne VI	401.146	0.17	401.941	0.22
Mg VIII	313.754	0.13	315.039	0.18
Si X	256.384	0.09	258.372	0.15
S XII	227.490	0.07 ($^2S_{1/2}$)	218.200	0.13
Ar XIV	194.401	0.08 ($^2S_{1/2}$)	187.962	0.12
Ca XVI	168.868	0.08 ($^2S_{1/2}$)	164.165	0.11
Fe XXII	117.144	0.08	114.409	0.09
n_j	Lower	Upper	Lower	Upper
2 – 3	$2s^22p (^2P_{1/2})$	$2s^23d (^2D_{3/2})$	$2s^22p (^2P_{3/2})$	$2s^23d (^2D_{5/2})$
Ion	λ (Å)	f	λ (Å)	f
C II	687.053	0.33	687.346	0.30
N III	374.198	0.44	374.434	0.39
O IV	238.360	0.50	238.570	0.45
Ne VI	122.516	0.56	122.701	0.50
Mg VIII	74.858	0.60	75.034	0.54
Si X	50.524	0.62	50.691	0.56
S XII	36.399	0.63	36.564	0.57
Ar XIV	27.469	0.64	27.631	0.58
Ca XVI	21.451	0.65	21.609	0.58
Fe XXII	11.767	0.67	11.921	0.59
n_j	Lower	Upper (†)	Lower	Upper
1 – 2	$2s^22p (^2P_{1/2})$	$1s2s^22p^2 (^2P_{3/2})$	$2s^22p (^2P_{3/2})$	$1s2s^22p^2 (^2P_{3/2})$
Ion	λ (Å)	f	λ (Å)	f
C II	43.050	0.13	43.049	0.17
N III	30.533	0.16	30.532	0.20
O IV	22.762	0.18	22.761	0.22
Ne VI	14.030	0.20	14.030	0.25
Mg VIII	9.500	0.22	9.500	0.28
Si X	6.853	0.23	6.853	0.29
S XII	5.179	0.25 ($^2D_{3/2}$)	5.174	0.30
Ar XIV	4.048	0.27 ($^2D_{3/2}$)	4.046	0.31
Ca XVI	3.249	0.29 ($^2D_{3/2}$)	3.247	0.31
Fe XXII	1.882	0.32 ($^2D_{3/2}$)	1.882	0.30

Notes. For the $2s - 2p$ ($n_j = 2 - 2$) and $1s - 2p$ ($n_j = 1 - 2$) transitions from the ground (lower) level, the upper level (denoted as †) vary for different elements (exceptions are marked following the f -values).

act values of τ_0 and EW also depend on the hydrogen column density (N_H) and turbulence velocity (v_b) of the ionized outflow.

4.2. Domain of density and ionization parameter diagnostics

Ions from different isoelectronic sequences cover an extensive area in the $n_H - \xi$ two dimensional parameter space. In Figure 7, each box corresponds to a certain ion. Within the box, the density of the plasma can be well constrained with lines from the metastable levels. Above (below) the box, only an lower (upper) limit can be obtained.

The box width gives the range of ionization parameter where lines from the ground and metastable levels are expected to be detected. The lower and upper boundaries correspond to $1/e$ of the maximum ion concentration using the AGN1 SED. Again we caution that a different ionizing SED yields different ionization parameter³.

The box height corresponds to the density of the plasma. The lower and upper boundaries of the box corresponds to 10% and 99% of the maximum metastable to ground level population ra-

³ Additionally, with the same ionizing SED, different photoionization codes (e.g. SPEX, XSTAR and Cloudy) yield different ionization parameter (see more details in Mehdipour et al. 2016)

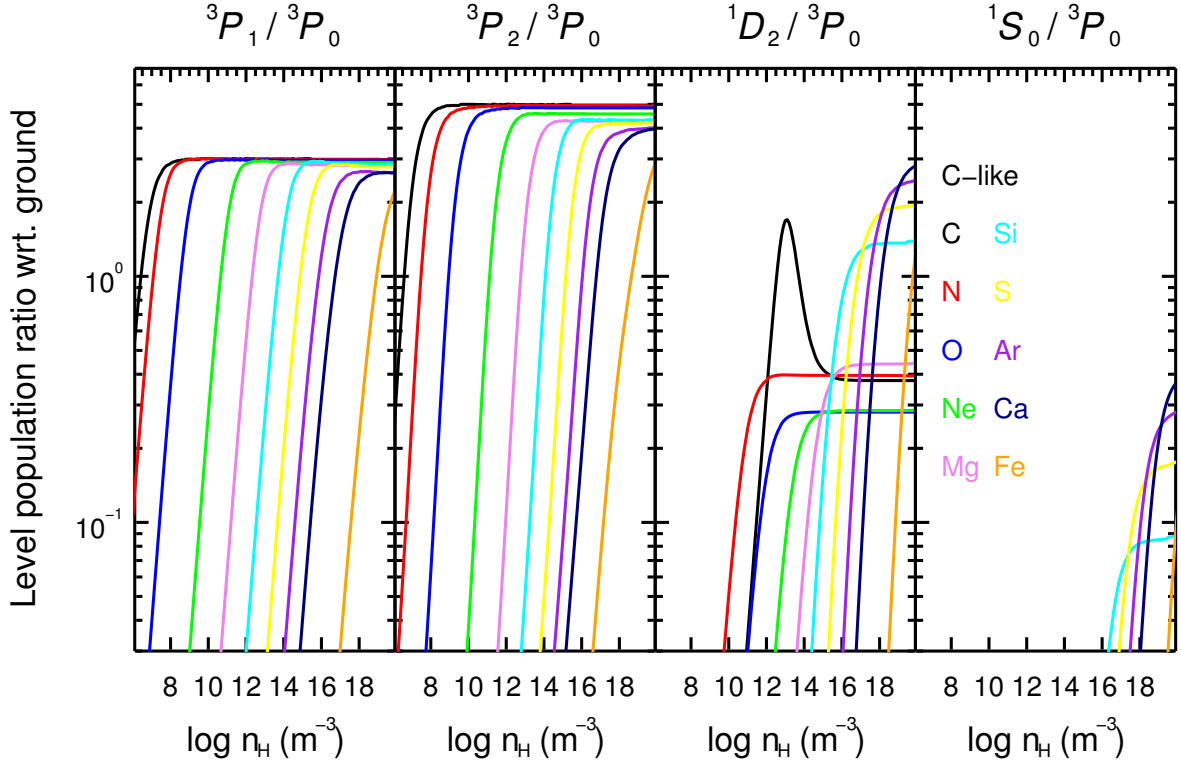


Fig. 4. Similar to Figure 2 but for C-like ions..

tio. Only the $2s^22p$ ($^2P_{3/2}$) metastable level in B-like ions and the $2s^22p^2$ (3P_1 and 3P_2) metastable levels in C-like ions are used for the calculation, since their corresponding metastable to ground EW ratios barely depend on the ionization parameter (Figure 6).

Be-like ions are not included in Figure 7 because the level population depends on both the ionization parameter (thus SED dependent) and density, as well as the metastable levels are less populated at the same density, compared to B-like and C-like ions (Section 3.4).

In addition, we also show the distance of the plasma inferred from the definition of ionization parameter (Equation 2). Within the same isoelectronic sequence, high- Z ions probe higher density, higher ionization parameter, and smaller distance, while low- Z ions measure lower density, lower ionization parameter, and larger distance. For ions in the same isonuclear sequence (i.e. same Z), less ionized ions can probe lower density, thus larger distance.

5. Density diagnostics for the ionized outflow in NGC 5548

NGC 5548 is the archetypal Seyfert 1 galaxy. As such, it exhibits all the typical spectral features seen in type 1 Seyfert galaxies. The broad band (from optical to hard X-ray) spectral energy distribution (SED) and various properties from the multiphase ionized outflow are well studied (e.g. Kaastra et al. 2014; Mehdipour et al. 2015b; Arav et al. 2015; Ebrero et al. 2016). NGC 5548 was observed with *Chandra* in January 2002 with both high and low energy transmission grating spectrometers (HETGS and LETGS), which allow us to study the X-ray absorption features in a wide wavelength range (~ 2 -60 Å).

Moreover, the 2002 spectra have the best signal-to-noise ratio of all high-resolution grating spectra of NGC 5548.

Here we re-analyse these spectra to search for density diagnostic lines. The HETGS (ObsID: 3046, with ~ 150 ks exposure) and LETGS (ObsID: 3383 and 3045, with ~ 340 ks total exposure) spectra are optimally binned (Kaastra & Bleeker 2016) and fitted simultaneously. Fits to LEG, MEG and HEG spectra are restricted to the 11–60 Å, 4–19 Å, and 1.8–10 Å wavelength range, respectively.

Six PION components are used to account for the six components in the ionized outflow (Kaastra et al. 2014; Ebrero et al. 2016). Assuming a low plasma density ($n_H = 10^6 \text{ m}^{-3}$ or 1 cm^{-3} , kept frozen) for all six PION components, the best-fit C-statistics are 5146.0 (denoted as the baseline C-statistics by the following), with a degree of freedom of 4843. The hydrogen column density (N_H), ionization parameter (ξ), turbulent velocity (v_b) and outflow velocity (v_{out}) for the PION components (Table 6) are consistent with values found in previous studies by Kaastra et al. (2014) and Ebrero et al. (2016).

For each PION component, we then vary its density from $n_H = 10^6 \text{ m}^{-3}$ to 10^{20} m^{-3} , with one step per decade. All the other parameters are kept frozen. The deviation of C-statistics (ΔC) from the baseline fit are demonstrated in Figure 8.

For the least ionized component A, the X-ray spectra with $\lambda \lesssim 60$ Å are insensitive to the density. The density sensitive lines that can be distinguished from the ground absorption lines of O IV (B-like) and Ne V (C-like) are at longer wavelength range ($\lambda \gtrsim 100$ Å, Table 3 and 4). That is to say, high-resolution UV spectra are required to determine the density for this component.

Meanwhile, we find a lower limit (at the confidence level of 3σ) of $n_H \gtrsim 10^{13} \text{ m}^{-3}$ for component B. Figure 9 shows the LETGS spectrum in the neighbourhood of Si IX absorption

Table 4. Characteristic absorption lines from the ground and the metastable levels in C-like ions.

Index	1		2		3		4	
n_j	Lower	Upper (†)	Lower	Upper (†)	Lower	Upper (†)	Lower	Upper
2 – 2	$2s^22p^2 (^3P_0)$	$2s2p^3 (^3S_1)$	$2s^22p^2 (^3P_1)$	$2s2p^3 (^3S_1)$	$2s^22p^2 (^3P_2)$	$2s2p^3 (^3S_1)$	$2s^22p^2 (^1D_2)$	$2s2p^3 (^1D_2)$
Ion	λ (Å)	f	λ (Å)	f	λ (Å)	f	λ (Å)	f
CI	1560.310	0.18 (3D_1)	1560.683	0.14 (3D_2)	1561.439	0.15 (3D_3)	1021.853	0.61
N II	644.634	0.25	644.837	0.25	645.179	0.25	775.966	0.36
O III	507.389	0.20	507.680	0.20	508.178	0.20	599.590	0.34
Ne V	357.947	0.15	358.475	0.15	359.374	0.15	416.212	0.27
Mg VII	276.154	0.12	277.001	0.12	278.402	0.12	319.027	0.22
Si IX	223.743	0.10	225.024	0.10	227.000	0.10	258.080	0.19
S XI	186.839	0.08	188.675	0.08	191.266	0.09	215.968	0.16
Ar XIII	236.268	0.08 (3D_1)	161.610	0.07	164.802	0.08	184.899	0.14
Ca XV	200.976	0.08 (3D_1)	140.583	0.06	144.309	0.07	161.018	0.12
Fe XXI	128.752	0.09 (3D_1)	142.149	0.05 (3D_2)	102.216	0.06	113.292	0.09
n_j	Lower	Upper	Lower	Upper	Lower	Upper	Lower	Upper
2 – 3	$2s^22p^2 (^3P_0)$	$2s^22p3d (^3D_1)$	$2s^22p^2 (^3P_1)$	$2s^22p3d (^3D_2)$	$2s^22p^2 (^3P_2)$	$2s^22p3d (^3D_3)$	$2s^22p^2 (^1D_2)$	$2s^22p3d (^1F_3)$
Ion	λ (Å)	f	λ (Å)	f	λ (Å)	f	λ (Å)	f
CI	1277.246	0.11	1277.283	0.08	1277.550	0.10	1463.337	0.10
N II	533.511	0.33	533.582	0.25	533.729	0.27	574.650	0.29
O III	305.596	0.54	305.656	0.37	305.768	0.41	320.978	0.46
Ne V	143.220	0.76	143.265	0.57	143.345	0.58	147.137	0.69
Mg VII	83.910	0.93	83.959	0.68	84.025	0.66	85.407	0.83
Si IX	55.305	1.05	55.356	0.74	55.401	0.71	56.027	0.91
S XI	39.240	1.13	39.300	0.74	39.323	0.73	39.648	0.97
Ar XIII	29.318	1.19	29.252	0.68	29.348	0.73	29.549	1.00
Ca XV	22.730	1.23	22.758	0.57	22.777	0.72	22.902	1.00
Fe XXI	12.292	1.24	12.433	0.43	12.331	0.59	12.411	0.94
n_j	Lower	Upper (†)	Lower	Upper (†)	Lower	Upper (†)	Lower	Upper (†)
1 – 2	$2s^22p^2 (^3P_0)$	$1s2s^22p^3 (^3D_1)$	$2s^22p^2 (^3P_1)$	$1s2s^22p^3 (^3P_1)$	$2s^22p^2 (^3P_2)$	$1s2s^22p^3 (^3D_3)$	$2s^22p^2 (^1D_2)$	$1s2s^22p^3 (^1D_2)$
Ion	λ (Å)	f	λ (Å)	f	λ (Å)	f	λ (Å)	f
CI	43.567	0.09	43.568	0.08 (3D_1)	43.568	0.08 (3D_1)	43.492	0.17
N II	30.963	0.11	30.944	0.10 (3S_1)	30.945	0.10 (3S_1)	30.914	0.21
O III	23.056	0.13 (3S_1)	23.057	0.11 (3S_1)	23.058	0.11 (3S_1)	23.061	0.24
Ne V	14.234	0.16	14.205	0.14 (3S_1)	14.237	0.12	14.211	0.28
Mg VII	9.604	0.19 (3S_1)	9.605	0.16 (3S_1)	9.628	0.14	9.611	0.30
Si IX	6.912	0.21 (3P_1)	6.914	0.18	6.929	0.14	6.916	0.32
S XI	5.225	0.24	5.218	0.19	5.229	0.15	5.220	0.33
Ar XIII	4.086	0.27	4.081	0.20	4.088	0.15	4.081	0.33
Ca XV	3.277	0.32	3.274	0.22	3.280	0.15	3.275	0.32
Fe XXI	1.895	0.44	1.894	0.22 (3S_1)	1.894	0.17 (1D_2)	1.894	0.19 (3P_2)

Notes. For the $2s - 2p$ ($n_j = 2 - 2$) and $1s - 2p$ ($n_j = 1 - 2$) transitions from the ground and metastable (lower) levels, the upper levels (denoted as †) vary for different element (exceptions are marked following the f -values).

Table 5. Values of $\log_{10}(\xi)$ where Be-like Si XI to C-like Si IX reach the maximum ion concentration in the ionization balance adopting different ionizing SED.

SED	AGN1	AGN2	PL
Si XI	1.90	2.03	1.90
Si X	1.72	1.94	1.71
Si IX	1.48	1.82	1.48

Notes. The three SEDs are adapted from [Mehdipour et al. \(2016\)](#). AGN1 and AGN2 refer to the SED of an archetypal Seyfert 1 galaxy NGC 5548 in normal and obscured state. PL refers to a SED that follows the power-law with $\Gamma = 2$.

lines (~ 56 Å), where the C-statistics are improved at high density. When $n_H \gtrsim 10^{13} \text{ m}^{-3}$, the population of the ground level $2s^22p^2 (^3P_0)$ decreases while the population of the metastable levels $2s^22p^2 (^3P_1$ and $^3P_2)$ increases (Figure 4). Accordingly, the ground absorption line at 56.15 Å (in the observed frame) is shallower while the metastable absorption lines at 56.20 Å and 56.25 Å are deeper. The 3σ upper limit of the distance of component B is accordingly 0.23 pc. The inferred density and distance disagree with the results reported in [Ebrero et al. \(2016\)](#), where a timing analysis (Section 1) is used. For the photoionized absorber component B, [Ebrero et al. \(2016\)](#) report $n_H \in (2.9, 7.1) \times 10^{10} \text{ m}^{-3}$ and $d \in (13, 20)$ pc, both at the

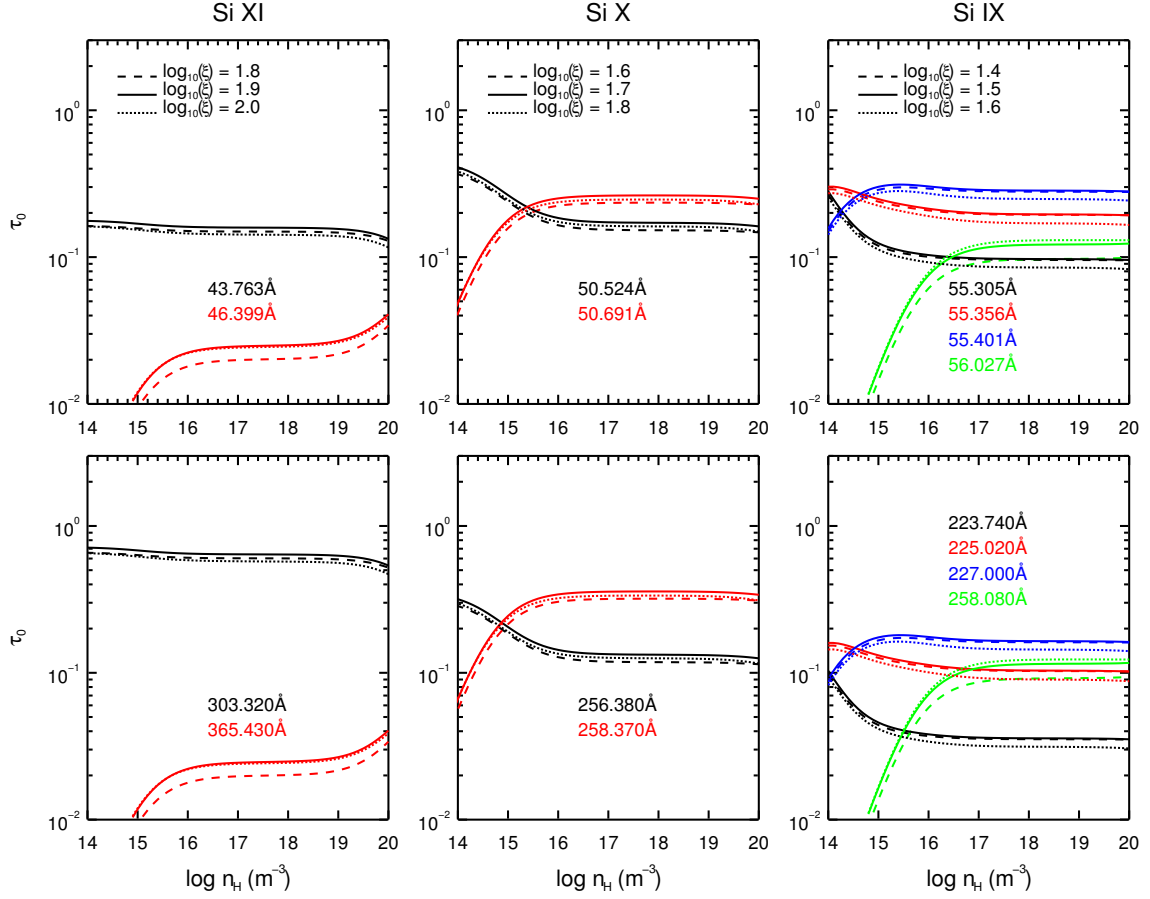


Fig. 5. Optical depth at the line centre (τ_0) for characteristic lines from ground and metastable levels in Be-like Si XI to C-like Si IX. The assumptions (SED, geometry, column density, turbulence, etc.) of the calculation are described in Section 2.

Table 6. Parameters of the six PION components in NGC 5548.

Component	A	B	C	D	E	F
N_H (10^{24} m^{-2})	2.6 ± 0.8	6.9 ± 0.9	10.8 ± 2.8	13.4 ± 2.1	25 ± 13	52.0 ± 8.5
$\log_{10}(\xi)$	0.51 ± 0.12	1.35 ± 0.06	2.03 ± 0.04	2.22 ± 0.03	2.47 ± 0.13	2.83 ± 0.03
v_b (km s^{-1})	150 ± 29	49 ± 14	40 ± 10	67 ± 17	6 ± 5	115 ± 29
v_{out} (km s^{-1})	-557 ± 37	-547 ± 35	-1108 ± 31	-271 ± 24	-670 ± 14	-1122 ± 34
n_H (m^{-3})	--	$\geq 10^{13}$	$\leq 10^{19}$	$\leq 10^{19}$	$\leq 10^{20}$	$\leq 10^{19}$

Notes. The lower or upper limits of the density (n_H) are at the confidence level of $\geq 3\sigma$, while the statistical uncertainties of all the other parameters are at the confidence level of 1σ .

confidence level of 1σ . The upper limits of density is based on the non-detection of variability on smaller timescales. Note that the authors also point out that there is a marginal hint of recombination time scale of ~ 4 and ~ 60 days, which would indicate a density lower limit (1σ) of $\sim 10^{10-11} \text{ m}^{-3}$, which would agree more with our results.

For components C – F, upper limits are obtained with $n_H \lesssim 10^{19} \text{ m}^{-3}$ (above 3σ for components C, E, and F) and $\lesssim 10^{20} \text{ m}^{-3}$ (2.6σ for component D). We show in Figure 10 the spectra in the neighbourhood of Fe XXII (B-like) and Fe XXI (C-like), with

the density of component F set to $n_H = 10^{10} \text{ m}^{-3}$ (left panels) and 10^{19} m^{-3} (right panels). At high density, the metastable absorption lines at 12.08 \AA (Fe XXII), at 12.50 \AA (Fe XXI) and 12.60 \AA (Fe XXI) are deeper. This overestimation of absorption lines contradicts with the data and leads to a poorer C-statistics. Of course, the spectra are crowded in this wavelength range, so that density diagnostics are challenging. The 3σ lower limits of the distance of components C – F are a few light-hours ($\sim 10^{12} \text{ m}$). The obtained density and distance for components

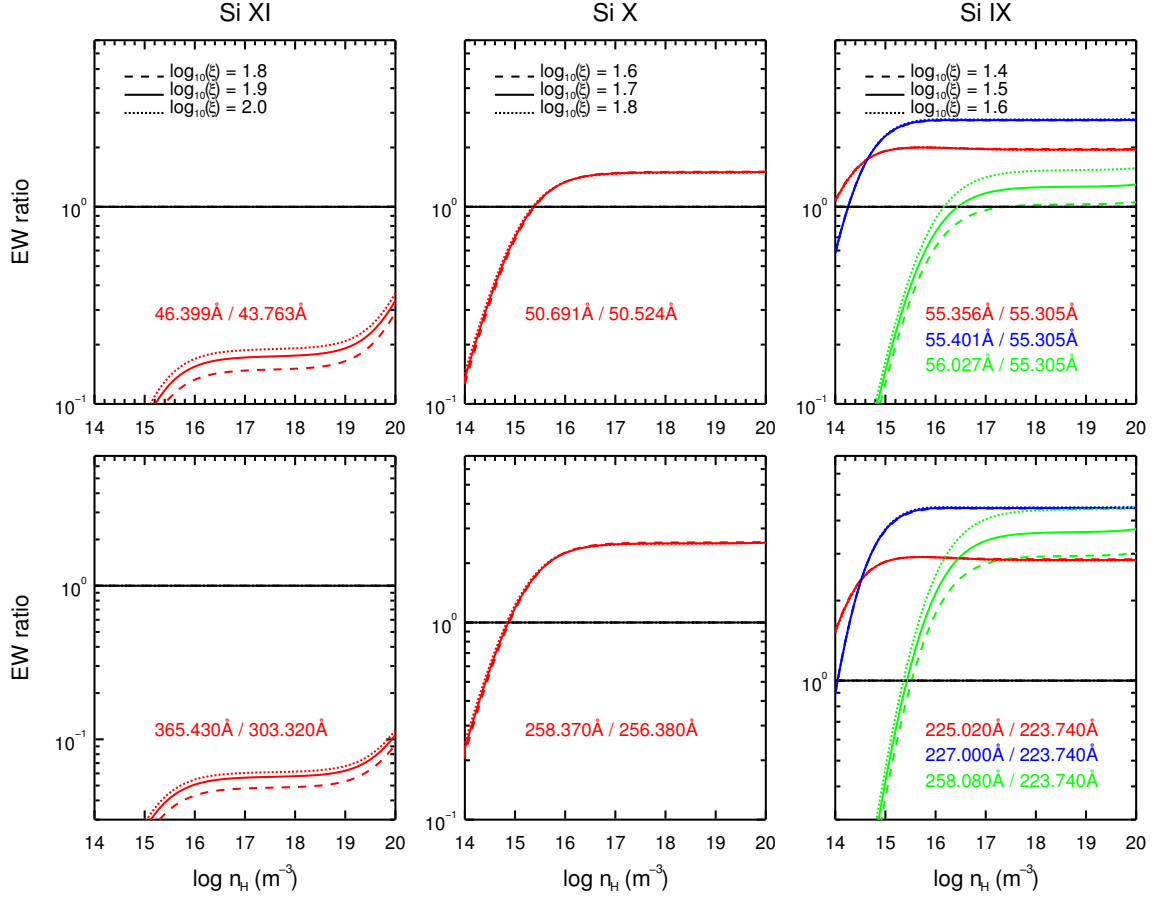


Fig. 6. Equivalent width (EW) ratios for characteristic lines from ground and metastable levels in Be-like Si XI to C-like Si IX. The assumptions (SED, geometry, column density, turbulence, etc.) of the calculation are described in Section 2. Note that for those lines with non-negligible optical depth ($\tau_0 \geq 1$), the exact EWs depend on the line broadening profiles.

C – F do not contradict the results ($n_H \gtrsim 10^{10} \text{ m}^{-3}$ and $d \lesssim 1 \text{ pc}$) reported in Ebrero et al. (2016).

Due to the narrow wavelength coverage and rather limited effective area of current grating instruments, and the lack of atomic data for N-like to F-like ions, density diagnostics using absorption lines from the metastable levels are not very effective. Once the N-like to F-like atomic data are included, a significant portion of the $n_H - \xi$ parameter space can be covered. Combined with the next generation of spectrometers onboard *Arcus* (Smith et al. 2016) and *Athena* (Nandra et al. 2013) will certainly identify the presence/absence of these density-sensitive absorption lines (Kaastra et al. 2017), thus tightly constraining the location and the kinetic power of AGN outflows. We refer the readers to Fig. 6 of Kaastra et al. (2017) for a simulated *Arcus* spectrum of NGC 5548, compared with the observed 2002 LETGS spectrum.

Acknowledgements. We thank the referee for constructive comments and suggestions. SRON is supported financially by NWO, the Netherlands Organization for Scientific Research.

References

Arav, N., Chamberlain, C., Kriss, G. A., et al. 2015, *A&A*, 577, A37

- Badnell, N. R. 2006, *ApJS*, 167, 334
 Bryans, P., Landi, E., & Savin, D. W. 2009, *ApJ*, 691, 1540
 Ciaravella, A., Raymond, J. C., Reale, F., Strachan, L., & Peres, G. 2001, *ApJ*, 557, 351
 Collinge, M. J., Brandt, W. N., Kaspi, S., et al. 2001, *ApJ*, 557, 2
 Del Zanna, G., Dere, K. P., Young, P. R., Landi, E., & Mason, H. E. 2015, *A&A*, 582, A56
 Ebrero, J., Kaastra, J. S., Kriss, G. A., et al. 2016, *A&A*, 587, A129
 Fabian, A. C. 2012, *ARA&A*, 50, 455
 Gallagher, P. T., Mathioudakis, M., Keenan, F. P., Phillips, K. J. H., & Tsinganos, K. 1999, *ApJ*, 524, L133
 Gu, M. F. 2008, *Canadian Journal of Physics*, 86, 675
 Kaastra, J. S., Mewe, R., & Nieuwenhuijzen, H. 1996, *UV and X-ray Spectroscopy of Astrophysical and Laboratory Plasmas*, 411
 Kaastra, J. S., Raassen, A. J. J., Mewe, R., et al. 2004, *A&A*, 428, 57
 Kaastra, J. S., Detmers, R. G., Mehdipour, M., et al. 2012, *A&A*, 539, A117
 Kaastra, J. S., Kriss, G. A., Cappi, M., et al. 2014, *Science*, 345, 64
 Kaastra, J. S., & Bleeker, J. A. M. 2016, *A&A*, 587, A151
 Kaastra, J. S. 2017, *Astronomische Nachrichten*, 338, 146
 Kaastra, J. S., Gu, L., Mao, J., et al. 2017, arXiv:1707.01251
 Kaspi, S., Brandt, W. N., Netzer, H., et al. 2001, *ApJ*, 554, 216
 Keenan, F. P., Conlon, E. S., Foster, V. J., Aggarwal, K. M., & Widing, K. G. 1993, *Sol. Phys.*, 145, 291
 Keenan, F. P., Pinfield, D. J., Woods, V. J., et al. 1998, *ApJ*, 503, 953
 Keenan, F. P., Katsiyannis, A. C., & Widing, K. G. 2004, *ApJ*, 601, 565
 King, A. L., Miller, J. M., & Raymond, J. 2012, *ApJ*, 746, 2
 Kramida, A., Yu. Ralchenko, Reader, J., and NIST ASD Team. 2015, *NIST Atomic Spectra Database (ver. 5.3, November 30, 2016)*. National

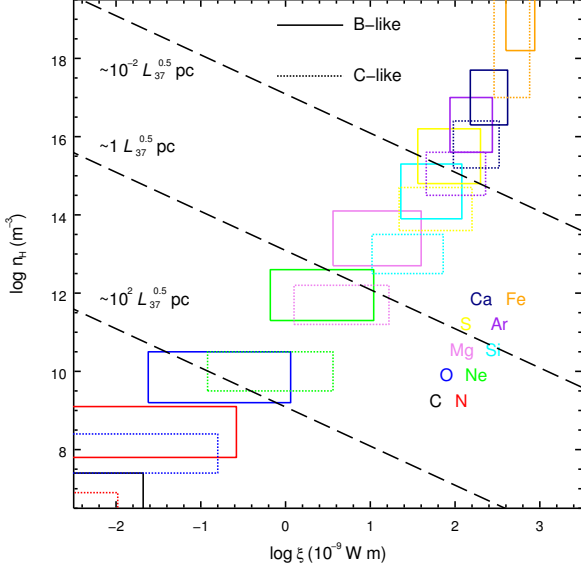


Fig. 7. Domain of density and ionization parameter where metastable absorption line from B-like (solid) and C-like (dotted) ions can be used for diagnostic in case of photoionized equilibrium. See Section 4.2 for detailed description. Dashed lines indicate the distance of the photoionized plasma with respect to the central engine. L_{37} is the 1 to 1000 Ryd luminosity in units of 10^{37} W.

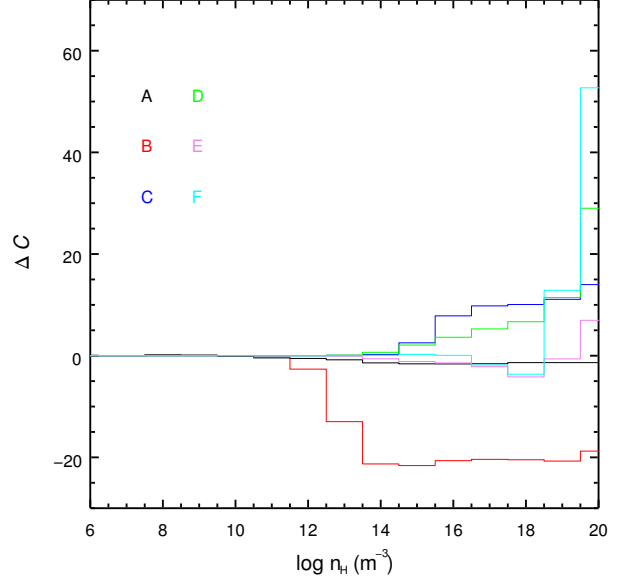


Fig. 8. The deviation of C-statistics (ΔC) from the baseline fit (C-stat. = 5146.0 and d.o.f. = 4843) with varying plasma density (n_H) for each photoionized absorber component (A–F). Component A refers to the least ionized photoionized absorber, and F refers to the most ionized photoionized absorber (Table 6).

- Institute of Standards and Technology, Gaithersburg, MD.
- Krolik, J. H., McKee, C. F., & Tarter, C. B. 1981, *ApJ*, 249, 422
- Landi, E., & Landini, M. 1998, *A&A*, 340, 265
- Landi, E., & Miralles, M. P. 2014, *ApJ*, 780, L7
- Lodders, K., Palme, H., & Gail, H.-P. 2009, *Landolt Börnstein*, 44
- Mao, J., & Kaastra, J. 2016, *A&A*, 587, A84
- McKernan, B., Yaqoob, T., George, I. M., & Turner, T. J. 2003, *ApJ*, 593, 142
- Miller, J. M., Raymond, J., Reynolds, C. S., et al. 2008, *ApJ*, 680, 1359-1377
- Mehdipour, M., Kaastra, J. S., & Raassen, A. J. J. 2015, *A&A*, 579, A87
- Mehdipour, M., Kaastra, J. S., Kriss, G. A., et al. 2015, *A&A*, 575, A22
- Mehdipour, M., Kaastra, J. S., & Kallman, T. 2016, *A&A*, 596, A65
- Nandra, K., Barret, D., Barcons, X., et al. 2013, *arXiv:1306.2307*
- Porquet, D., Dubau, J., & Grosso, N. 2010, *Space Sci. Rev.*, 157, 103
- Schurch, N. J., Warwick, R. S., Griffiths, R. E., & Kahn, S. M. 2004, *MNRAS*, 350, 1
- Silva, C. V., Uttley, P., & Costantini, E. 2016, *A&A*, 596, A79
- R. K. Smith R. K., Abraham M. H., Allured R., Bautz M., Bookbinder J., et al. 2016, *Proc. SPIE 9905*, <http://dx.doi.org/10.1117/12.2231778>
- Tarter, C. B., Tucker, W. H., & Salpeter, E. E. 1969, *ApJ*, 156, 943
- Warren, H. P., & Warshall, A. D. 2002, *ApJ*, 571, 999
- Warren, H. P., & Brooks, D. H. 2009, *ApJ*, 700, 762
- Urdampilleta, I., Kaastra, J. S., & Mehdipour, M. 2017, *A&A*, 601, A85

Appendix A: N-like Fe XX to F-like Fe XVIII

Currently, in SPEXACT v3.04, the atomic data for the N-like to F-like isoelectronic sequences are lacking, except for Fe XX, Fe XIX, and Fe XVIII. We repeat the same analyses described above for N-like to F-like Fe here. For both N-like Fe XX and O-like Fe XIX, the first four excited levels can be populated up to a few tens of percent, compared to the ground level population, while only the first excited level of F-like Fe XVIII can be populated significantly (Figure A.1). Characteristic transitions from these ground and metastable levels are listed in Table A.2.

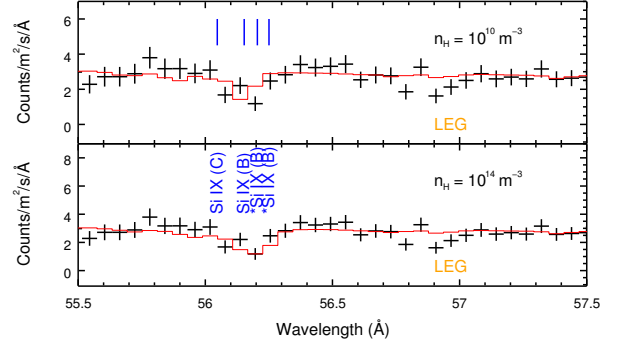


Fig. 9. PION modelling of the LEG spectrum of NGC 5548 with $n_H = 10^{10} \text{ m}^{-3}$ (upper panel) and 10^{14} m^{-3} (lower panel). The spectral bin size is 0.025 Å. The overall C statistics is 5146.0 (d.o.f. = 4843) at low density and 5124.7 (d.o.f. = 4842) at high density. The two density sensitive metastable absorption lines of Si IX (C-like), from component B, at 55.20 Å and 56.25 Å (in the observed frame) are labelled with *.

Comparing the density-sensitive metastable levels for Be-like Fe XXIII to F-like Fe XVIII (Figure A.1), we find that, in general, the metastable levels in C-like Fe XXI can be more easily populated when $n_H \gtrsim 10^{16} \text{ m}^{-3}$. In addition, when $n_H \lesssim 10^{16} \text{ m}^{-3}$, the first excited level $2s^2 2p^4 (^3P_0)$ of O-like Fe XIX can be populated up to 10% of the ground level population, which has been pointed out in Kaspri et al. (2001). Nonetheless, the density-sensitive line (13.420 Å) of O-like Fe XIX is rather weak, compared to the ground level absorption lines (13.521 Å and 13.492 Å). Meanwhile, the density-sensitive line (13.420 Å)

Table A.1. Characteristic absorption lines from the ground and metastable levels in N-like to F-like iron ions.

Index		1		2		3	
Sequence	n_j	Lower	Upper	Lower	Upper	Lower	Upper
Fe XX	2-2	$2s^2 2p^3 (^4S_{3/2})$	$2s 2p^4 (^4P_{5/2})$	$2s^2 2p^3 (^2D_{3/2})$	$2s 2p^4 (^2D_{3/2})$	$2s^2 2p^3 (^2D_{5/2})$	$2s 2p^4 (^2P_{3/2})$
Fe XX	2-3	$2s^2 2p^3 (^4S_{3/2})$	$2s^2 2p^2 (^3P) 3d (^4P_{3/2})$	$2s^2 2p^3 (^2D_{3/2})$	$2s^2 2p^2 (^3P) 3d (^2D_{5/2})$	$2s^2 2p^3 (^2D_{5/2})$	$2s^2 2p^2 (^3P) 3d (^2F_{3.5})$
Fe XX	1-2	$2s^2 2p^3 (^4S_{3/2})$	$1s 2s^2 2p^4 (^4P_{5/2})$	$2s^2 2p^3 (^2D_{3/2})$	$1s 2s^2 2p^4 (^2D_{3/2})$	$2s^2 2p^3 (^2D_{5/2})$	$1s 2s^2 2p^4 (^2D_{5/2})$
Fe XIX	2-2	$2s^2 2p^4 (^3P_2)$	$2s 2p^5 (^3P_2)$	$2s^2 2p^4 (^3P_0)$	$2s 2p^5 (^3P_1)$	$2s^2 2p^4 (^3P_1)$	$2s 2p^5 (^3P_2)$
Fe XIX	2-3	$2s^2 2p^4 (^3P_2)$	$2s^2 2p^3 (^2D) 3d (^3D_3)$	$2s^2 2p^4 (^3P_0)$	$2s^2 2p^3 (^2P) 3d (^3P_1)$	$2s^2 2p^4 (^3P_1)$	$2s^2 2p^3 (^2D) 3d (^3D_2)$
Fe XIX	1-2	$2s^2 2p^4 (^3P_2)$	$1s 2s^2 2p^5 (^3P_2)$	$2s^2 2p^4 (^3P_0)$	$1s 2s^2 2p^5 (^3P_1)$	$2s^2 2p^4 (^3P_1)$	$1s 2s^2 2p^5 (^3P_2)$
Fe XVIII	2-2	$2s^2 2p^5 (^2P_{3/2})$	$2s 2p^6 (^2S_{1/2})$	$2s^2 2p^5 (^2P_{1/2})$	$2s 2p^6 (^2S_{1/2})$	--	--
Fe XVIII	2-3	$2s^2 2p^5 (^2P_{3/2})$	$2s^2 2p^4 (^1D) 3d (^2D_{5/2})$	$2s^2 2p^5 (^2P_{1/2})$	$2s^2 2p^4 (^1S) 3d (^2D_{3/2})$	--	--
Fe XVIII	1-2	$2s^2 2p^5 (^2P_{3/2})$	$1s 2s^2 2p^6 (^2S_{1/2})$	$2s^2 2p^5 (^2P_{1/2})$	$1s 2s^2 2p^6 (^2S_{1/2})$	--	--

Table A.2. Characteristic absorption lines from the ground and the metastable levels in N-like Fe xx to F-like Fe xviii (SPEXACT v3.04).

Index		1		2		3	
Ion	n_j	λ (Å)	f	λ (Å)	f	λ (Å)	f
Fe XX	2-2	132.850	0.05	110.626	0.08	93.782	0.09
Fe XX	2-3	12.835	0.48	12.984	0.60	12.885	0.87
Fe XX	1-2	1.908	0.15	1.906	0.24	1.906	0.15
Fe XIX	2-2	108.355	0.06	109.952	0.08	119.983	0.03
Fe XIX	2-3	13.521	0.73	13.420	1.23	13.735	0.50
Fe XIX	1-2	1.918	0.15	1.918	0.23	1.921	0.10
Fe XVIII	2-2	93.923	0.06	103.937	0.05	--	--
Fe XVIII	2-3	14.203	0.88	14.121	0.86	--	--
Fe XVIII	2-1	1.928	0.11	1.931	0.11	--	--

of O-like Fe XIX is sensitive to both ionization parameter and density (Figure A.2). Additionally, from the observational point of view, we caution that the $n_j = 2 - 3$ transitions of Fe XVIII at 14.203 Å (ground) and 14.121 Å (metastable) might be blended with the O VIII absorption edge at 14.228 Å.

Appendix B: Comparison of the level population calculation with CHIANTI

CHIANTI (Del Zanna et al. 2015) is a widely used atomic code for analysing emission line spectra from astrophysical sources. The CHIANTI code provides similar detailed calculations such as level populations, as the SPEX code does. Therefore, here we compare the level population calculations for collisional ionized equilibrium (CIE) plasmas, using the latest version of CHIANTI v8.0.8 (with atomic database v8.0.6⁴) and SPEX v3.04 (with SPEXACT v3.04) to show the effects of different atomic code.

For simplicity, we only compare the population of the first five levels (i.e. the ground level and the first four excited levels) of the Fe isonuclear sequence from He-like Fe XXV to Ne-like Fe XVII. The level populations are calculated in both codes using the same abundance table (Lodders et al. 2009), same ionization balance (Bryans et al. 2009), and same plasma temperature (where the ion concentration reaches its maximum). Figure B.1 shows the level population ratio with respect to the ground as a function of plasma density ranging from 10^6 m^{-3} to 10^{20} m^{-3} (or 10^1 cm^{-3} to 10^{14} cm^{-3}).

For He-like Fe XXV and Li-like Fe XXIV, the level population ratios provided by the two codes are consistent with each

other. For Be-like Fe XXIII to Ne-like Fe XVII, the level population ratios share the same increasing and/or flattening trend, whereas the two codes yield slightly different (a factor of few) level population ratios. This is not totally unexpected, given the fact that the two codes do not use the same atomic data for individual atomic processes, and the two codes use different ways of implementation of the atomic data for the calculation (interpolation or parameterization). For instance, the CHIANTI atomic database includes various atomic data with $n \leq 5$ for almost all ions with $Z \leq 30$ in the He-like to Ne-like isoelectronic sequences, while the SPEXACT includes atomic data with $n \leq 8$ for He-like to C-like ions with $Z \leq 30$, and only Fe ions in the N-like to Ne-like isoelectronic sequences. The atomic data collected in both codes are state-of-the-art, yet still incomplete and not 100% accurate. Furthermore, the SPEX code parameterizes almost all the atomic data (e.g. Mao & Kaastra 2016; Urdampilleta et al. 2017), while CHIANTI use interpolation instead.

In short, considering only the systematic uncertainties introduced by the different atomic data used in SPEX and CHIANTI, with the same density diagnostics in Be-like to Ne-like ions, the two codes are expected to estimate the plasma density to a similar order of magnitude. However, it is not clear which part(s) of the atomic data and/or code contribute to what percentage of the total “error” (i.e. the discrepancy between the codes) budget for the level population calculation of a specific level in a specific ion.

⁴ <http://www.chiantidatabase.org/>

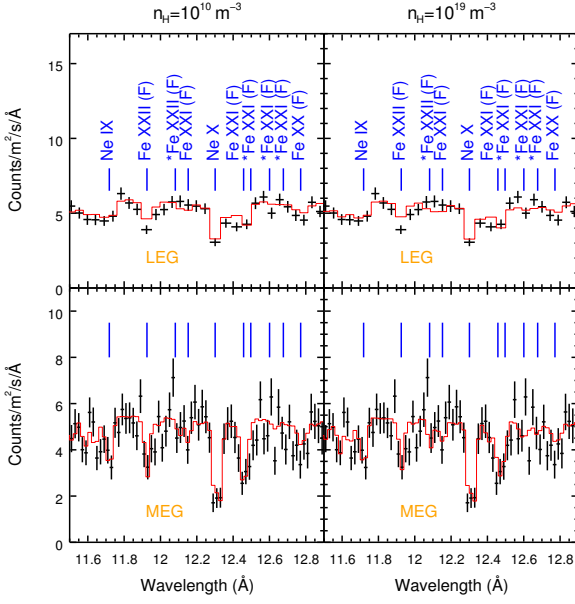


Fig. 10. PION modelling of the spectra of NGC 5548 with $n_{\text{H}} = 10^{10} \text{ m}^{-3}$ (left panels) and 10^{19} m^{-3} (right panels). The spectral bin sizes are 0.025 \AA (for LEG) and 0.01 \AA (for MEG), respectively. The overall C statistics is 5146.0 (d.o.f. = 4843) at low density and 5158.9 (d.o.f. = 4842) at high density. The density sensitive metastable absorption lines of Fe XXII (B-like) and Fe XXI (C-like), from component F, are labelled with *.

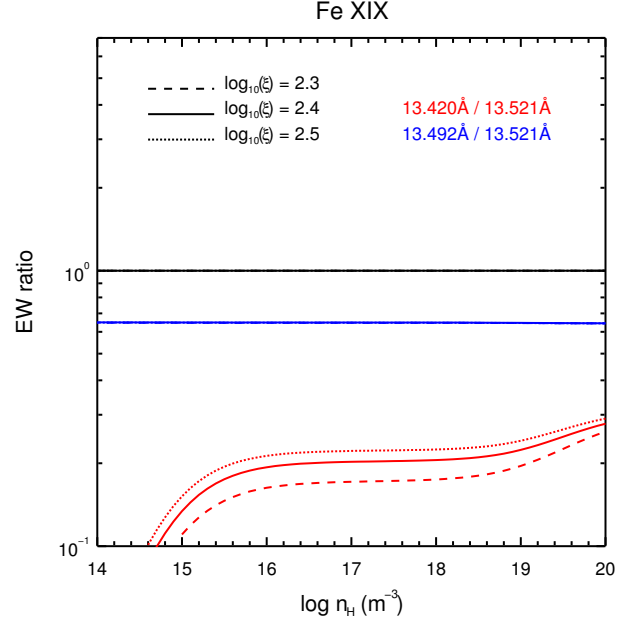


Fig. A.2. Equivalent width (EW) ratios for characteristic absorption lines of O-like Fe XIX. The two lines with $\lambda = 13.521 \text{ \AA}$ and 13.492 \AA are from the ground level. The line with $\lambda = 13.420 \text{ \AA}$ is from the first excited level. Dashed ($\xi = 2.3$), solid ($\xi = 2.4$), where ion concentration reaches its maximum, and dotted ($\xi = 2.5$) lines indicate different ionization parameters of the photoionized plasma.

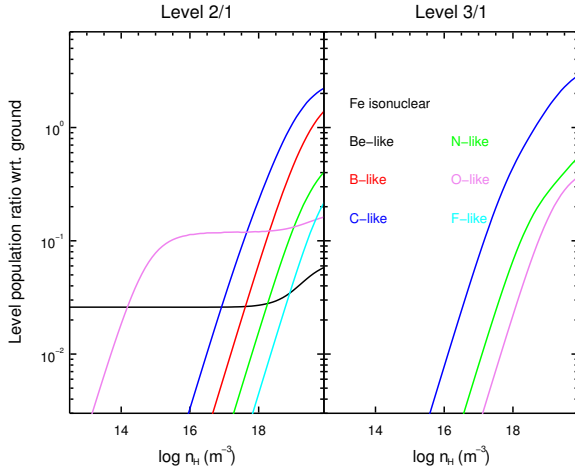


Fig. A.1. Metastable to ground level population ratio as a function of density of the Fe isonuclear sequence (from Be-like to F-like), at the temperature of maximum ion concentration in ionization equilibria. The configuration and $2S+1L_J$ notation of the ground (Level 1) and metastable levels (Level 2 and 3) are listed in Table 1.

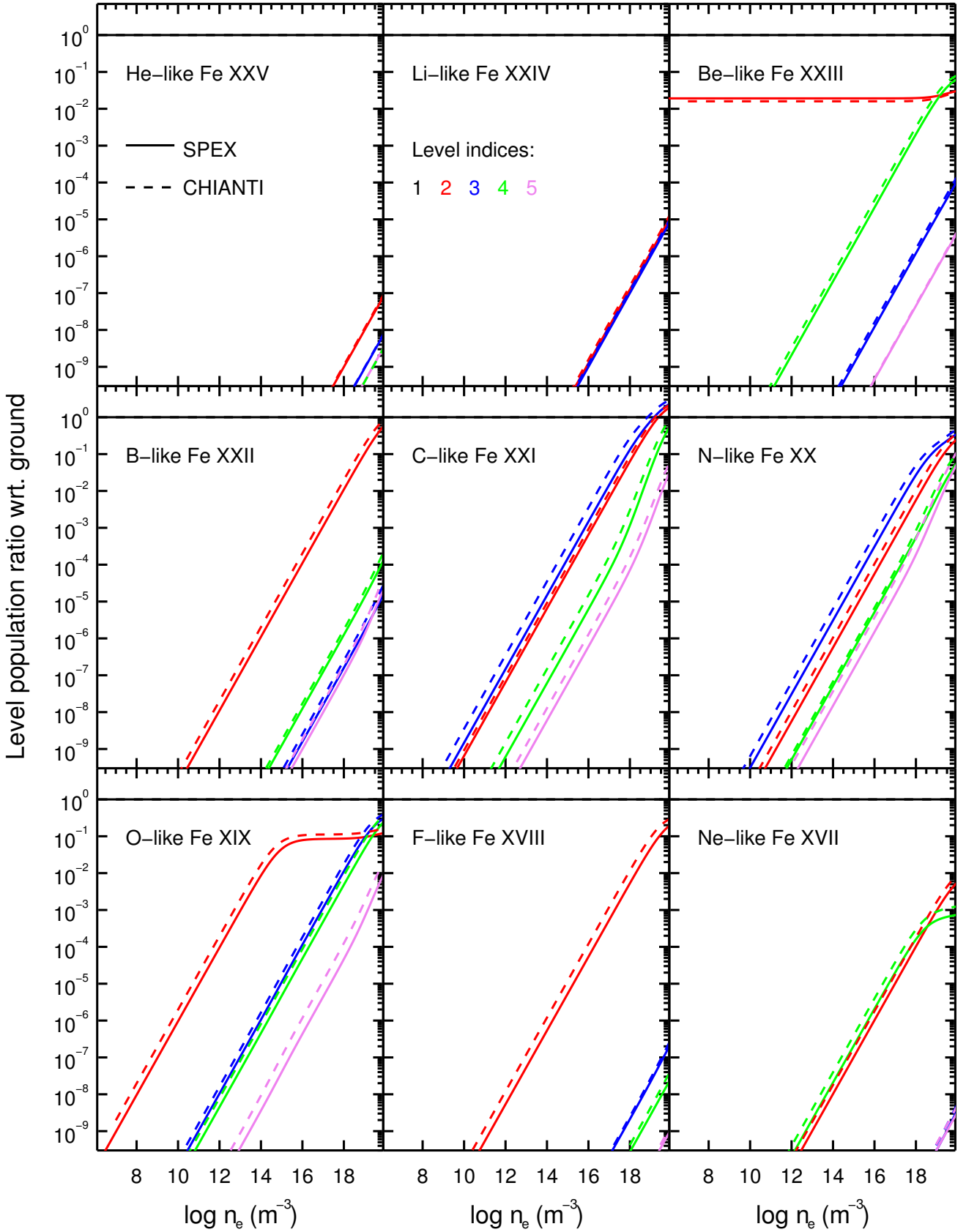


Fig. B.1. The level population ratio for the first four excited levels (level indices 2–5) of the Fe ionization sequence from He-like Fe XXV to Ne-like Fe XVII for collisional ionized equilibrium (CIE) plasma, using SPEXACT v3.04 (solid line) and CHIANTI v8.0.8 (dashed line). The CHIANTI atomic database v8.0.6 is used.